

# Experimental control of compressible OA209 dynamic stall by air jets

A.D. Gardner<sup>\*</sup>, K. Richter<sup>†</sup>, H. Mai<sup>‡</sup>, D. Neuhaus<sup>§</sup>

## ABSTRACT

The experimental investigation of constant blowing air jets as Fluidic Control Devices (FCDs) for helicopter dynamic stall control is described. A carbon fibre airfoil of constant OA209 cross-section was fitted with a pneumatic system to deliver dry compressed air as jets for flow control at total pressures of up to 10 bar. The experiment used porthole jets of radius 1% chord, positioned at 10% chord and with spacing 6.7% chord. The positive dynamic stall control effects were demonstrated at Mach 0.3, 0.4 and 0.5 for deep dynamic stall test cases with the best test cases reducing the pitching moment peak after the main stall by 84%, while increasing the mean lift over one pitching cycle by 37%. The conclusions from the experiments are supported by 3D URANS computations of the pitching airfoil with flow control using the DLR-TAU code.

## NOMENCLATURE

$\alpha$	Angle of attack ( $^{\circ}$ )
$b$	Airfoil model breadth ( $=0.997$ m)
$c$	Airfoil chord ( $=0.300$ m)
$C_L$	Lift coefficient
$C_D$	Drag coefficient
$C_M$	Pitching moment coefficient
$C_P$	Pressure coefficient
$C_{P-crit}$	Pressure coefficient for $M=1.0$
$C_{\mu}$	Momentum ratio jets/freestream
$C_q$	Mass flux ratio jets/freestream
$f$	Frequency (Hz)
$\gamma$	Ratio of specific heats ( $=1.4$ )
$L_{act}$	Breadth of model with actuation ( $=0.84$ m)
$M$	Mach number
$\dot{m}_m$	Mass flux for the model (kg/s)
$P_j$	Total pressure of the jet air (bar)
$R$	Gas constant for air ( $=287$ J/kg/K)
$Re$	Reynolds number based on the model chord
$\rho_{\infty}$	Freestream flow density ( $\text{kg/m}^3$ )
$s$	spacing of the jets in $y$ -direction (m)
$t$	Time (s)
$T_0$	Total temperature of the jet air (K)
$v_{\infty}$	Freestream flow velocity (m/s)
$v_j$	Jet velocity (m/s)
$\omega^*$	Reduced frequency: $\omega^* = 2\pi f c / v_{\infty}$

<sup>\*</sup>Corresponding Author. German Aerospace Center (DLR), Institute of Aerodynamics and Flow Technology, Bunsenstrasse 10, 37073 Göttingen, Germany. [tony.gardner@dlr.de](mailto:tony.gardner@dlr.de)

<sup>†</sup>DLR-Institute of Aerodynamics and Flow Technology

<sup>‡</sup>DLR Institute of Aeroelasticity

<sup>§</sup>DLR Institute of Materials Physics in Space

$x$	Coordinate in flow direction (m)
$y$	Ordinate in breadth (m)
$z$	Ordinate vertically upward (m)

## INTRODUCTION

Dynamic stall is a well-known effect for helicopter airfoils occurring when a pitching airfoil stalls, forming separated flow in a dynamic stall vortex. A lift peak and a negative spike in pitching moment form and then a rapid drop in lift appears as the stall vortex moves downstream. The torsional impulse from the pitching moment peak is often a load-limiting case for the pitch links of the helicopter rotor blades, and high drag is experienced compared to attached flow. The DLR-ONERA project SIMCOS is part of a long-term German-French cooperation to combat dynamic stall (DS) and improve numerical modelling with regards to dynamic stall. As part of this project the effect of pulsed and constant blowing jets on dynamic stall is being investigated both experimentally and numerically, with this paper describing the experimental investigation of constant blowing on an OA209 airfoil in the Transonic Wind Tunnel Göttingen (DNW-TWG), as shown in Figure 1.



Figure 1: The OA209-FCD model installed in the adaptive-wall test section of the DNW-TWG.

The investigation of passive devices for dynamic stall control on the OA209 airfoil [4] in the project SIMCOS showed considerable success, with Leading Edge Vortex Generators (LEVoGs) showing up to 50% reduction in the pitching moment peak at Mach 0.14 [10], and around 25% reduction at Mach 0.3 and 0.4 [13]. Also in SIMCOS, Deployable Vortex Generators (DVGs) showed a reduction in the pitching moment peak of up to 55% at Mach 0.16 [3]. Similar experiments by Martin et al. using vane vor-

tex generators [14], showed a strong control effect at Mach 0.3. Unfortunately, of these experiments, only Martin et al. investigated dynamic stall control for increased Mach numbers including flow separation dominated by a strong shock, and in this case no good control was achieved. It is desirable to have a flow control method which will be effective over the entire range Mach 0.1 to Mach 0.5, and not have a critical Mach number or angle of attack dependence.

Passive control devices, as described above, use energy from the oncoming flow to affect the flow. In contrast, active control devices have an external energy source, which increases the maximum possible control of the flow. One type of active control device is blowing by jets out of the surface of the airfoil. Water tunnel experiments using active blowing by Weaver et al. [19] have shown that active blowing can have results significantly better than for passive generators. Experiments in a low-speed wind tunnel [18] showed that good dynamic stall control due to pulsed blowing is also possible in air.

In the preparation of the present work, a CFD design process was used with the blowing rates of Weaver et al. scaled to Mach 0.3 and different jet geometries were investigated to find the optimal geometry for dynamic stall with constant blowing [8] and with pulsed blowing [5].

## EXPERIMENTAL ARRANGEMENT

A carbon fibre model (Figure 1) with chord length 0.300 m and breadth 0.997 m was produced for the 1 m x 1 m adaptive wall test section of the DNW-TWG in a similar configuration to that used for other dynamic stall investigations [7]. The model was constructed of two carbon-fibre half-shells, an aluminium spar and aluminium mounting feet (Figure 2). Dry compressed air was supplied to jets at a maximum total pressure of 10 bar, and maximum flow rate of  $\dot{m}_m=0.25$  kg/s for  $L_{act}=0.84$  m of actuated model. Cavities in the spar distributed the air to 42 portholes of 3 mm (1% chord) diameter positioned at 10% chord. Pressure and acceleration instrumentation were mounted on the inside of the carbon-fibre shells, and the pressure system was integrated into the aluminium spar and controlled by cylindrical valves screwed into the spar.

Figure 3 shows a schematic of the pressure system. Dry compressed air at between 1 bar and 50 bar is supplied to the system. Outside the test section, the mass flux was measured using a Systec DF12 mass flux measurement system, based on differential pressure over a calibrated strut, temperature and pressure measurement (MT). Inside the aluminium spar of the model, the pressure is reduced by flow through four orifices (O1-O4), and the pressure (PT) and temperature (TT) of the system is measured. Finally, the air with pressure between 1 and 10 bar is supplied to valves V1-V42, screwed into the spar. The valves were developed by the DLR [15, 16] and can be individually switched on and off, and pulsed at frequencies of up to 500 Hz. The air was ejected from the airfoil surface using portholes of

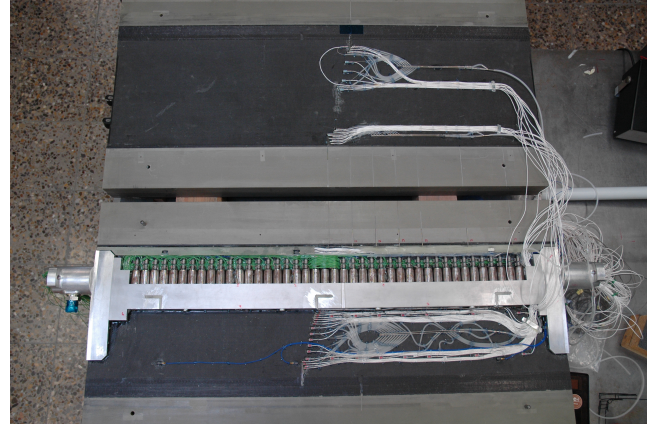


Figure 2: The two half-shells of the OA209-FCD model before closing.

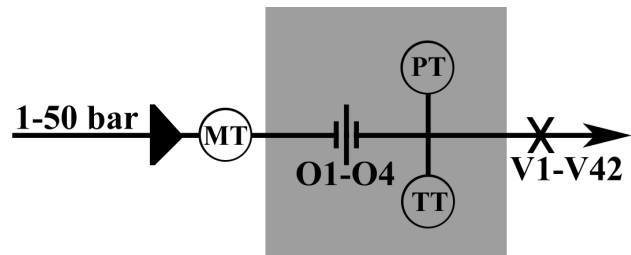


Figure 3: Schematic of the pneumatic system.

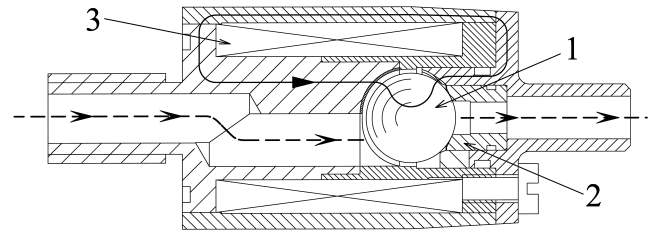


Figure 4: Fast switching valve shown in the closed state. The closed dark line with the arrow shows the magnetic flux in the valve. The broken line with the arrows shows the path of the gas through the valve.

3 mm diameter at 10% chord, flush with the airfoil surface. The jets resulting from these portholes were directed normal to the airfoil chord line on the suction side of the airfoil and had a spacing of 6.7% chord (20 mm).

In Figure 4 a drawing of the fast switching valve is shown. A single 8 mm diameter magnetisable valve ball (1) is the closure element of the valve, and its only moving part. Only the pressure difference between valve inlet and valve outlet keeps the ball in the valve seat (2). To open the valve the magnetic coil (3) generates a magnetic field, which is guided by magnetisable material in the housing of the valve. The magnetic field generates a force on the ball which rolls the ball off the valve seat. The force acts mainly perpendicular to the valve axis. When the magnetic field is switched off, the flow carries the ball back on the

valve seat and the valve closes.

The model was mounted horizontally in the adaptive-wall test section of the DNW-TWG wind tunnel and driven with pitch-oscillations from drive shafts through the side-walls attached at the quarter-chord position. The adaptive test section has flexible top and bottom walls which were statically adapted at the mean angle of attack of the model to minimise the interference velocities at the wall. Hydraulic motors, located outside the test section, drove the model from both sides. The model was moved with a strong pitching motion at amplitudes  $4\text{-}7^\circ$  and frequencies  $2\text{-}5.7\text{ Hz}$  at Mach numbers  $0.3\text{-}0.5$ . A phase-locked data acquisition system, sampled each sensor with 1024 points per period for 160 periods. The model was equipped with a line of 49 Kulite unsteady pressure sensors (type XCQ-093), at an angle of  $10^\circ$  to the oncoming flow, near the centerline. The sensors were situated to guarantee a maximum discretisation error of 1% in lift, pressure-drag and pitching moment computed from the pressure taps during static measurements and dynamic stall without blowing. The discretisation error was estimated in the design phase by comparing discretised and non-discretised data for a given pressure sensor distribution using around 2000 computed dynamic and static pressure distributions for each airfoil. A further 20 pressure sensors were distributed spanwise over the upper surface of the model to investigate 3D effects of the dynamic stall process.

In addition, drag was measured for static points without blowing using a wake rake, which only delivered valid measurements when there was no mass-addition into the flow. The model deformation and position was measured using a PicColor stereoscopic point-tracking system. The angle of attack was measured using laser triangulators at the ends of the model. An array of control accelerometers, angle meters and force balances ensured that maximal structural loads on the model were not exceeded during the experiments.

## NUMERICAL METHOD

Computations using the DLR-TAU code are presented for a 3D slice of breadth 20% chord of the dynamically pitching OA209 airfoil using periodic boundaries, using the method described in [8]. Unsteady Reynolds-averaged Navier-Stokes (URANS) computations were undertaken with the DLR-TAU code [9]. The node-based finite-volume solver was used on a hybrid unstructured grid consisting of prismatic layers close to the viscous surfaces and a tetrahedral field, generated using the Centaur<sup>TM</sup>[2] unstructured grid generator.

The computations used settings found in a previous study [17] which produced results which compared well with experiment. The computations were fully turbulent using the Spalart-Allmaras turbulence model, a central scheme with a scalar dissipation method, and a lower upper symmetric Gauss-Seidel (LUSGS) implicit flux solver

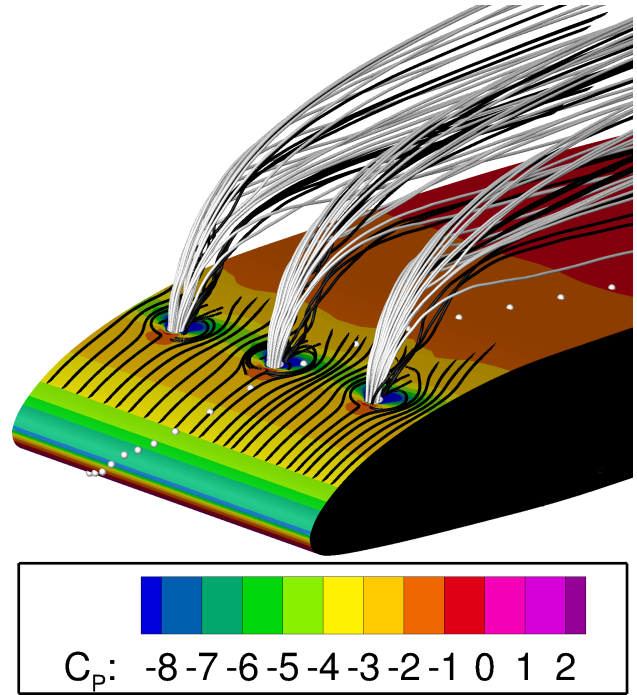


Figure 5: CFD result showing the complex 3D flow.

was used, with no multigrid convergence acceleration and a CFL number of 2. The URANS computations used 1600 time steps per period with 400 inner iterations per time-step. A minimum of 3 pitching cycles needed to be computed for convergence, with convergence of the computation assumed when the difference between the lift, pitching moment and drag for the second and third cycles were within pre-defined tolerances, approximately equal to 1% of the value at the minimum angle of attack computed.

The grid was generated according to the guidelines of Richter et al. [17] for grid convergence on this geometry and test condition, with grid cells of 1% chord on the top and bottom of the airfoil and finer cells of 0.15% on the leading and trailing edges and around the jets. The 3D grids had around 2 million points. Additional 2D RANS computations at static angle of attack, providing static drag values, used a grid similar to the 2D grid in [17].

## DATA ANALYSIS

The experimental lift, pitching moment and drag are integrated from the pressure transducers on the model surface. These were positioned using 2D computations assuming uniform flow across the y-coordinate (breadth) of the airfoil model. While this is accurate for test cases without blowing, when the jets are turned on, the situation becomes more complex.

Figure 5 shows a CFD result for pitching at  $\alpha=13\pm 7^\circ$  with  $M=0.30$ ,  $Re=1.15e6$ , at  $\alpha=14.4^\circ$  on the upstroke. The surface  $C_p$  is indicated with coloured contours, showing that a second suction peak appears between the jets, which



Figure 6: Oil flow picture for  $M=0.3$ ,  $Re=1.15e6$ ,  $\alpha=13^\circ$ ,  $P_j=10$  bar. Flow is from left to right.

is not uniform over the  $y$ -coordinate. Volume streamlines have been placed to illustrate the flow, with the white streamlines being material from the jets, and dark lines material from the freestream. The acceleration of material from the freestream out of the separated region behind the jets leads to a local decrease in  $C_p$  behind the jets, and the flow blockage between the jets causes a local decrease in  $C_p$  between the jets. Particularly the re-expansion of the flow from a constriction between the jets is experimentally observed in oil-flow pictures at constant angle of attack (Figure 6) before the vortex footprint starts to expand on the surface.

In Figure 5 the experimental sensor positions are noted with white spheres. It is desirable to know whether the integration of the pressure signals will result in a reliable estimate of the integral force over the surface. Figure 7 compares the pressure distribution at this condition extracted from the locations of the pressure sensors in the CFD, with the pressure distribution obtained by averaging slices of the CFD solution at constant  $x/c$  across the breadth of the computational domain. The method of averaging slices yields a pressure distribution which can be integrated to yield the true forces for the 3D flow. For this CFD point, the discretisation error in lift was +8% including the sensor at  $x/c=0.11$ , and the inclusion of the sensor at  $x/c=0.11$  better reproduces the qualitative shape of the pressure distribution. In Figure 8, the single-sensor peak is matched qualitatively between experiment and CFD at  $\alpha=14.4^\circ$  on the upstroke, indicating that this sensor should be used.

The forces on the model, calculated from the pressure sensors, need to be corrected for the momentum force due to the air jets. This force is

$$(1) \quad F = \dot{m}_m / L_{act} \sqrt{\frac{2\gamma RT_0}{\gamma + 1}}.$$

The jet is assumed sonic at the surface of the model, and  $T_0$ , the total temperature, is assumed to be equal to the measured temperature of the aluminium spar in the model. Further,  $\dot{m}_m$  is the mass flux as measured by the DF12 mass flux sensor,  $L_{act}=0.84$  m is the breadth of model which is acted upon by the actuation jets, and  $\gamma=1.4$  and

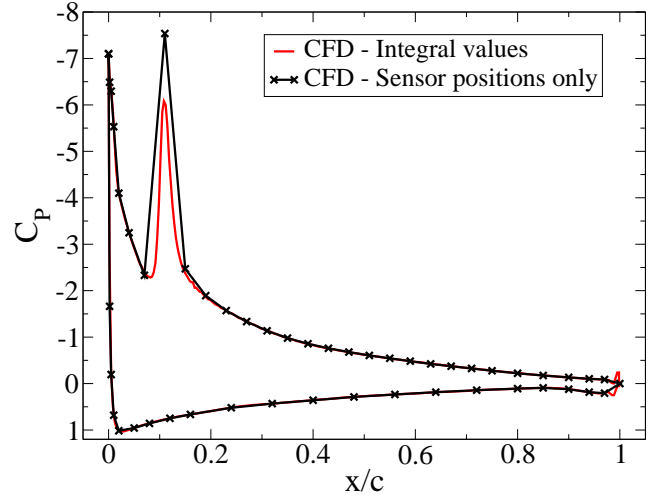


Figure 7: Comparison of CFD data for different discretisations.

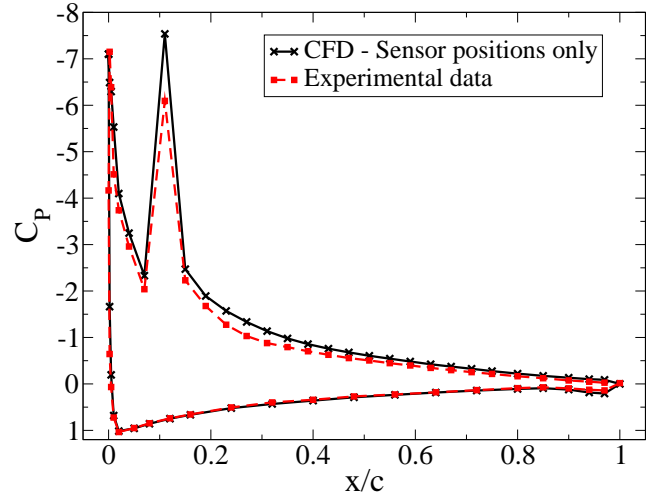


Figure 8: Comparison of CFD data for the experimental sensor positions, and experiment.

$R=287$  J/kg/K are the gas constants for dry compressed air. The corrected values of the lift, drag and pitching moment coefficients are computed from their uncorrected values, assuming that the jet force is directed normal to the model chord in a downward direction, at  $x/c=0.10$ .

Variables were phase averaged over 160 cycles of 1024 points to get a mean and standard deviation for each point on the cycle. The experimental data is presented with angle of attack uncorrected for wind tunnel effects, geometry changes in the model compared to the nominal airfoil or other effects. The standard deviation in  $\alpha$  was less than  $0.05^\circ$ , and so is not plotted. Additionally, the mean lift and mean pitching moment over a cycle were taken for each dynamic point by averaging the data over all cycles. The pitching moment peak is taken as the difference between the value of the phase-averaged coefficient, at the peak and “flat” value a short time beforehand, as in [8], to compensate for the general shift in the pitching moment values which occurs with blowing.

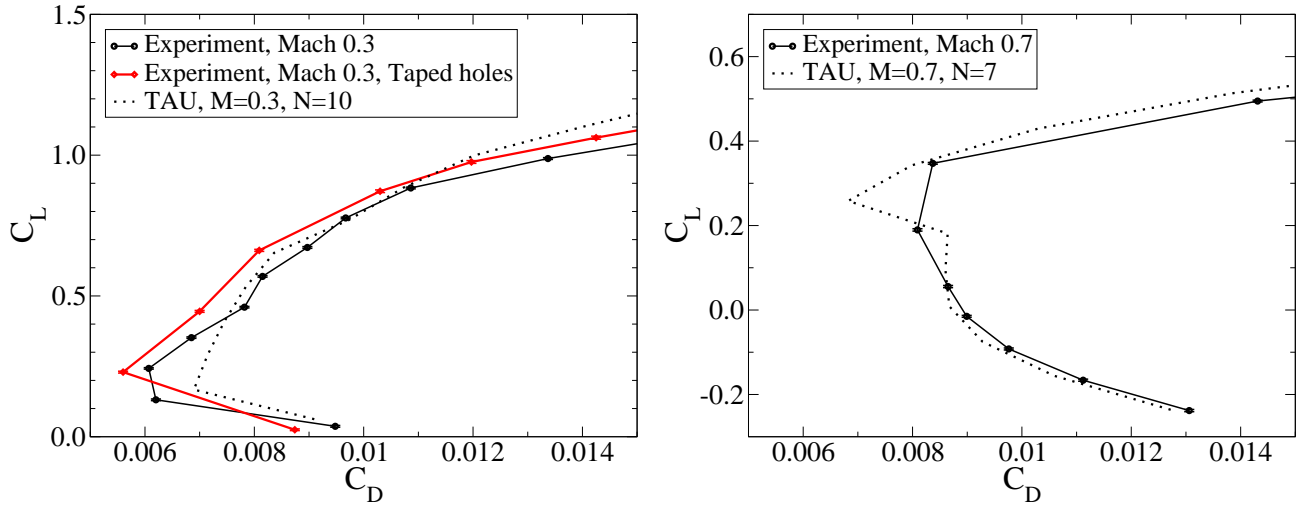


Figure 9: Comparison of OA209 static drag polars without blowing and comparison to CFD with transition prediction. Shown for  $M=0.7$ ,  $Re=2.7e6$  (Left) and  $M=0.3$ ,  $Re=1.15e6$  (Right).

The repeatability of mean lift over a pitching cycle and peak lift was better than 3% for test points which were nominally identical. The repeatability of the pitching moment peak value was within 12% for test points which were nominally identical. The standard deviation of the phase-averaged data is shown for every 16th point on all figures.

The flow control with constant blowing scales with the mass flux ratio ( $C_q$ ) or the momentum ratio ( $C_\mu$ ) between the jets and the freestream.  $C_\mu$  and  $C_q$  are defined for compressible flow [8] as:

$$(2) \quad C_\mu = \frac{2}{cL_{act}} \frac{\dot{m}_m v_j}{\rho_\infty v_\infty^2},$$

$$(3) \quad C_q = \frac{\dot{m}_m}{\rho_\infty v_\infty cL_{act}},$$

with  $\dot{m}_m$  the mass flux out of the jets and  $v_j$  the jet velocity, set to be a constant  $M=1.0$ .

## RESULTS AT STATIC ANGLE OF ATTACK

Figure 9 shows drag polars taken at Mach 0.3 and 0.7, compared with TAU computations with  $e^N$  transition prediction as described in [11]. The N-factors of  $N=10$  and  $N=7$  for  $M=0.3$  and  $M=0.7$  respectively are computed from the measured turbulence levels in the DNW-TWG using the method of Mack [12], as detailed in AGARDograph 793 [1]. Since the portholes of 3 mm diameter potentially cause early boundary layer transition, the transition behaviour was investigated by comparing drag measurements on the airfoil with experiments where the holes are covered by a silicon-backed Teflon tape of thickness  $62 \mu\text{m}$ . This tape was thinner than the  $90\text{--}120 \mu\text{m}$  required to cause boundary layer transition at these conditions. Experimentally, the complete drag was measured using a wake rake. In Figure 9 (left) the model has a lower drag when the holes are

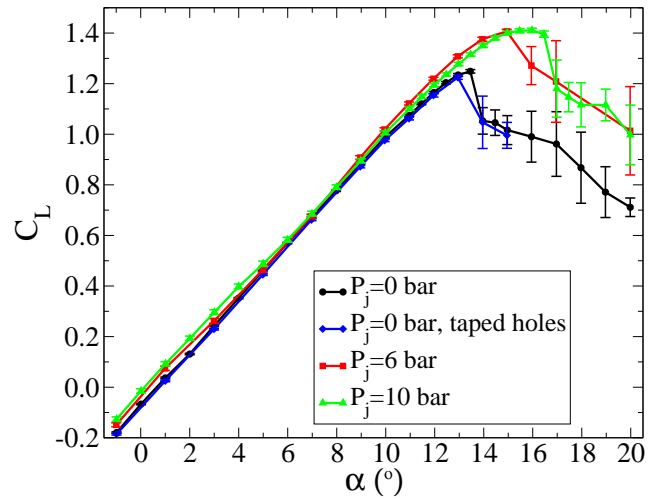


Figure 10: Lift polars with and without constant blowing at  $M=0.3$ ,  $Re=1.15e6$ .

covered with tape, but that the drag is consistently lower than a computation with transition. Additionally, a laminar dip is present in the experimental data, indicating that the laminarity of the boundary layer is only quantitatively (by a maximum of eight drag counts) and not qualitatively affected by the addition of the portholes. Likewise, at Mach 0.7 (Figure 9, right), the drag is not significantly different to the computed drag, indicating that no significant drag penalty is to be expected from the addition of portholes onto the airfoil

Lift polars were measured at Mach 0.3 with and without constant blowing through all portholes (Figure 10). In the normal case without blowing, the lift increases monotonically up a maximum lift of  $C_L=1.25$  at  $\alpha=13.45^\circ$  with a small RMS value. The flow then separates and the lift decreases monotonically with increased unsteadiness compared with the attached flow, up to the maximum angle measured at  $\alpha=20^\circ$ . The polar with tape over the holes

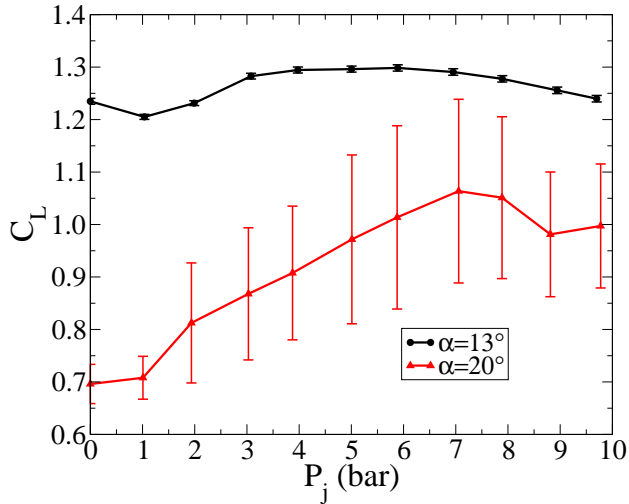


Figure 11: Lift variation with constant blowing pressure at constant angle of attack at  $M=0.3$ ,  $Re=1.15e6$ .

appears to stall earlier (at  $\alpha=12.74^\circ$ ), but this polar was measured with fewer points, so a point is missing compared with the case without tape. Since the existing points agree well with each other, we conclude that the portholes did not affect the maximum lift within the accuracy with which we measured.

When constant blowing was used, the maximum lift increased by 12.8% to  $C_L=1.41$  for both  $P_j=6$  bar ( $C_\mu=0.069$ ,  $C_q=0.010$ ) and 10 bar ( $C_\mu=0.12$ ,  $C_q=0.017$ ). In addition, the lift at  $\alpha=20^\circ$  increased by approximately 40% over the lift for the case without blowing. In comparison, CFD during the design phase [5] predicted a 37% increase using RANS and a 48% increase using URANS, for blowing at  $P_j=6.7$  bar.

If the angle of attack is now held constant, and the pressure is increased, a pressure polar is obtained (Figure 11). For this flow condition, at  $P_j=10$  bar,  $C_\mu=0.12$  and  $C_q=0.017$ , and these scale linearly with pressure. At  $\alpha=20^\circ$  and at low pressures, increasing the blowing pressure results in an increase in the lift, until at  $P_j=7$  bar an increase in lift of 52% is observed compared to the case with no blowing. After this, the lift reduces, or remains approximately constant with increasing pressure. Similarly, for  $\alpha=13^\circ$  with attached flow, a maximum improvement of 7.7% in lift is seen at  $P_j=6$  bar, although the decrease at  $P_j=7$  bar is minimal. It appears, then that for the static flow, the improvement in the aerodynamics for constant blowing has a maximum at  $P_j=6$  to 7 bar, decreasing thereafter.

### DYNAMIC STALL AT MACH 0.3

Figure 12 shows data for the pitching dynamic stall airfoil without blowing for the condition  $M=0.3$ ,  $Re=1.15e6$ ,  $f=5.7$  Hz ( $\omega^*=0.11$ ),  $\alpha=13\pm 7^\circ$ . The OA209 airfoil shows leading edge stall with a strong dynamic stall vortex, followed by unsteady separated flow. The three points noted with  $\alpha=13\pm 7^\circ$  were measured on three consecutive days

and are all nominally the same test condition. An increased variance between the nominally identical points is seen at the point of stall, with a maximum difference in mean lift over a cycle of 1.1% between cases and in peak lift of 2.8% between cases. The difference in the pitching moment peak is larger, with a difference of 10.6% between outliers.

Additionally, Figure 12 shows experimental data taken in 2004 [13] for a different OA209 wind tunnel model at nominally the same conditions. The height of the first pitching moment peak in the older data is 40% higher than in the new data, and the second pitching moment peak seen in the old data is not present in the newer data. The source of this large difference in the pitching moment is unclear at present. The most probable source of the discrepancy is a difference in the movement on the model centerline between the two experiments, due to the motors driving the model or due to the model elasticity

As shown in other experiments [7], the effect of higher ramping rate at the moment of separation is similar to the effect of increasing the oscillation frequency, in that higher ramping rates lead to an increase in the angle of attack at which lift-stall occurs, and an increased pitching moment peak. Figure 13 (Left) compares the angle of attack history at the model ends for the old and new data, to the nominal sine signal at  $M=0.3$ ,  $Re=1.15e6$ ,  $f=5.7$  Hz ( $\omega^*=0.11$ ),  $\alpha=13\pm 7^\circ$ . On the upstroke, the new experiment shows a higher ramping rate, which is associated with stronger dynamic stall, and the sine-signal is not followed as well due to the significantly higher weight of the model with valves compared to the older model. Other experimental data in [7] suggests that for the EDI-M109 airfoil doubling the pitching frequency at similar conditions results in a 40% increase in the pitching moment peak. Thus with a pure sine motion the new data would have an even lower peak than it currently does. At  $16^\circ \leq \alpha \leq 18^\circ$ , the part of the movement curve relevant for the separation, the motions are similar between the old and new data sets.

The motion of the new model at the centerline of the wind tunnel was measured using a PicColor stereo pattern recognition system using the white dots visible in Figure 1. The surface position was measured at 23 points and compared with wind-off data by a linear fit of the point positions to acquire values for the model heave and pitching angle at 256 points per pitching cycle. Due to the lower sampling rate of the stereoscopic data, every fourth point is shown, rather than every sixteenth for the laser triangulator data. Since the model heave and pitch were also measured at each end of the model by laser triangulators, a comparison between these two pitching values gives the elastic torsion of the model due to the angular momentum and aerodynamic forces. In Figure 13 (Right), for the new model, the maximum difference between the angle of attack at the two positions is  $0.34^\circ$ . The difference for the older experiment is unknown. The older wind tunnel model was also made of carbon fibre, but the improvement in materials and modelling led to the design of a considerably stiffer structure for the new model.

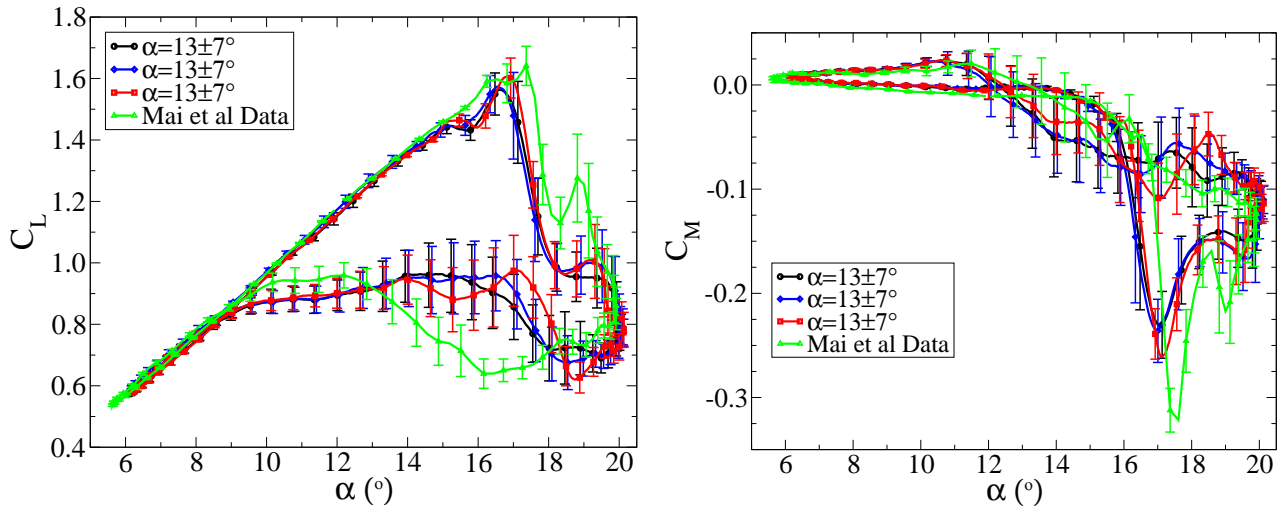


Figure 12: Comparison of airfoil data without blowing, showing experimental variation and the difference to an older experiment [13]. Shown is lift (Left) and pitching moment coefficient (Right).

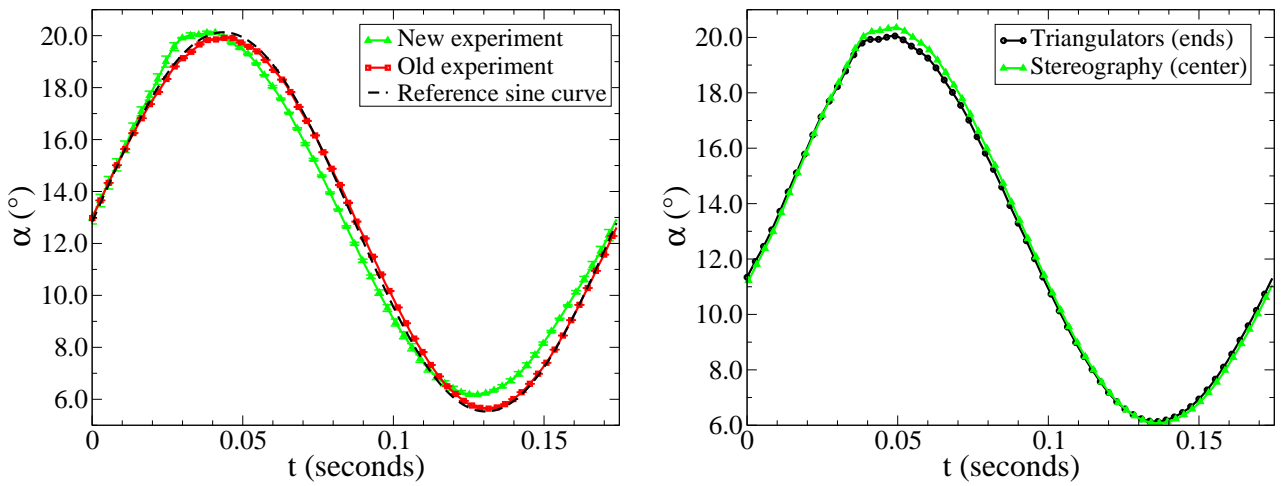


Figure 13: Comparison of: (Left) the angle of attack history for the old and new experimental OA209 data without blowing (Right) the angle of attack at the model ends and at the model centerline for the new data.

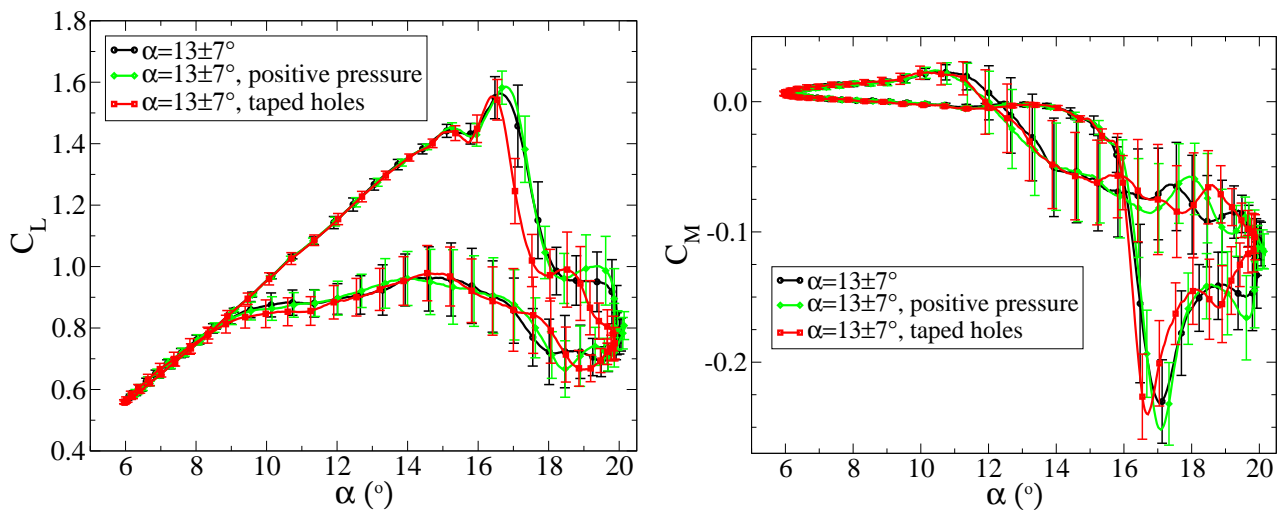


Figure 14: Comparison of airfoil data without blowing, showing experimental variation due to tape and valve leakage. Shown is lift (Left) and pitching moment coefficient (Right).

Figure 14 shows the variation in the forces due to the installation of tape over the blowing holes at  $M=0.3$ ,  $Re=1.15e6$ ,  $f=5.7$  Hz ( $\omega^*=0.11$ ),  $\alpha=13\pm 7^\circ$ . The same silicon-backed Teflon tape of thickness  $62\ \mu\text{m}$  was used as in the cases with static angle of attack. Figure 14 shows that the case with taped holes has earlier separation, by around  $\Delta\alpha=-0.5^\circ$  compared with the reference case, but the pitching moment peak is relatively unchanged. To observe the effects of the residual leakage in the valves, which is relevant for cases when pressure is applied but not all valves are open, a residual pressure of 2 bar was applied when all valves were closed. The result, as shown in Figure 14, is that the difference observed remained within the scatter. Thus the valves were working as expected, and the tests with constant blowing could continue.

### FLOW CONTROL AT MACH 0.3

The flow control effect with constant blowing is illustrated in Figure 15 for  $P_j=3$  bar ( $C_\mu=0.035$ ,  $C_q=0.005$ ),  $P_j=6$  bar ( $C_\mu=0.069$ ,  $C_q=0.010$ ) and  $P_j=10$  bar ( $C_\mu=0.12$ ,  $C_q=0.017$ ), compared with the reference case with no blowing. Data is for  $M=0.3$ ,  $Re=1.15e6$ ,  $f=5.7$  Hz ( $\omega^*=0.11$ ),  $\alpha=13\pm 7^\circ$ . Blowing at  $P_j=3$  bar causes worse dynamic stall than no blowing, with an increase in the pitching moment peak of 41% compared with the reference case. The jets strengthen the two leading edge stall vortices, causing the large pitching moment peaks. Despite this, the mean lift over a pitching cycle increased by 9.3%. If the blowing is increased to  $P_j=6$  bar ( $C_\mu=0.069$ ,  $C_q=0.010$ ), an improvement in the dynamic stall behaviour is observed, with the pitching moment peak reduced by 51%, but at this condition the secondary stall peak is stronger than the initial peak, and this second peak is only 22% reduced from the reference case. This is because the initial stall is a trailing edge stall, which is then followed by a stronger leading edge stall causing the large second stall peak. At  $P_j=10$  bar ( $C_\mu=0.12$ ,  $C_q=0.017$ ), both the primary and secondary stall peak are about the same size, and the pitching moment peak is reduced by 59% over the reference case. A pure trailing edge stall is seen, with the flow in front of the jets not stalling at all.

The effect of the dynamic stall control by the jets at  $P_j=10$  bar in Figure 15 is to slow down the dynamic stall process, so that although it starts at  $\alpha=16^\circ$  as for the case without blowing, the peak pitching moment is reached at  $\alpha=18.5^\circ$  rather than at  $\alpha=17^\circ$  for the reference case. This slowed separation has the effect, as noted in the design study [8], of producing a significantly weaker dynamic stall vortex and thus causing lower pitching moments. The slowing of the stall is also seen at  $P_j=6$  bar, but less strongly.

As a comparison, a similar pressure variation was computed using URANS (Figure 16). A dynamic stall control effect is achieved, which is qualitatively similar to that seen in the experiment. A much stronger dynamic stall control effect is seen, with an 86% reduction in the pitch-

ing moment peak at  $P_j=6.7$  bar, which is significantly more than seen in the experiments. Further, the flow control at  $P_j=3.35$  bar is significant, whereas in the experiment at similar pressures a net negative effect is seen. Unfortunately instead of the increased slowing of the stall with increasing blowing seen in the experiments, the stall is faster with increasing blowing in the computations. Although the general dynamic stall control effect is predicted by the CFD, the prediction requires more investigation of the grid and turbulence model than the settings which were primarily chosen in the experiment design phase to yield good engineering approximations at acceptable computational cost.

Despite the downward force from the jet at 10% chord and the data from CFD, the pitching moment for the experiment during the attached flow becomes more positive due to the altered aerodynamics on the airfoil. Figure 17 (Left) shows that the positive pitching moment is caused by the additional suction peak formed between the jets. The critical pressure is exceeded, but the flow appears not to behave like the shock-induced separations seen at higher Mach numbers. After stall, at the point of minimum pitching moment (Figure 17, Right), the pitching moment of the cases with blowing is increased by the preservation of a suction plateau in front of the jets, and by increasing the pressure on the surface behind the jets, probably due to reducing the strength of the dynamic stall vortex. The suction plateau is also the reason for the significantly increased lift after stall when constant blowing is used (Figure 15). The mean lift over a cycle increases by 14% for  $P_j=10$  bar compared to the reference case without blowing.

As a comparison, the leading edge vortex generators (LEVoGs) of Mai et al. [13] were attached to the model and tested without blowing (Figure 18). The LEVoGs reduced the pitching moment peak by 24% and increased the mean lift by 4%. It should be emphasised that despite the lower effectiveness of the LEVoGs compared with the blowing, that the blowing required a full model to be built at considerable expense, whereas the LEVoGs required 15 minutes to glue onto the leading edge.

### INVESTIGATION OF OPTIMUM PRESSURE AND JET SPACING

In contrast to the static test cases at constant  $\alpha=20^\circ$ , where a saturation of the positive effect was seen at  $P_j=7$  bar, no saturation of the dynamic stall control effect was noted at  $M=0.3$  and  $Re=1.15e6$ . Unfortunately, at  $Re=1.15e6$  the maximum pressure of the pneumatic system was reached at 10 bar, so to further increase  $C_\mu$  and  $C_q$ , the Reynolds number was reduced to  $Re=575000$ . At this Reynolds number, the blowing coefficients at  $P_j=5$  bar ( $C_\mu=0.12$ ,  $C_q=0.019$ ) are roughly equivalent to those at  $Re=1.15e6$  and  $P_j=10$  bar ( $C_\mu=0.12$ ,  $C_q=0.017$ ), and an equivalent trailing edge dynamic stall is seen for  $P_j \geq 5$  bar. In Figure 19, the data without blowing looks slightly different to that at higher

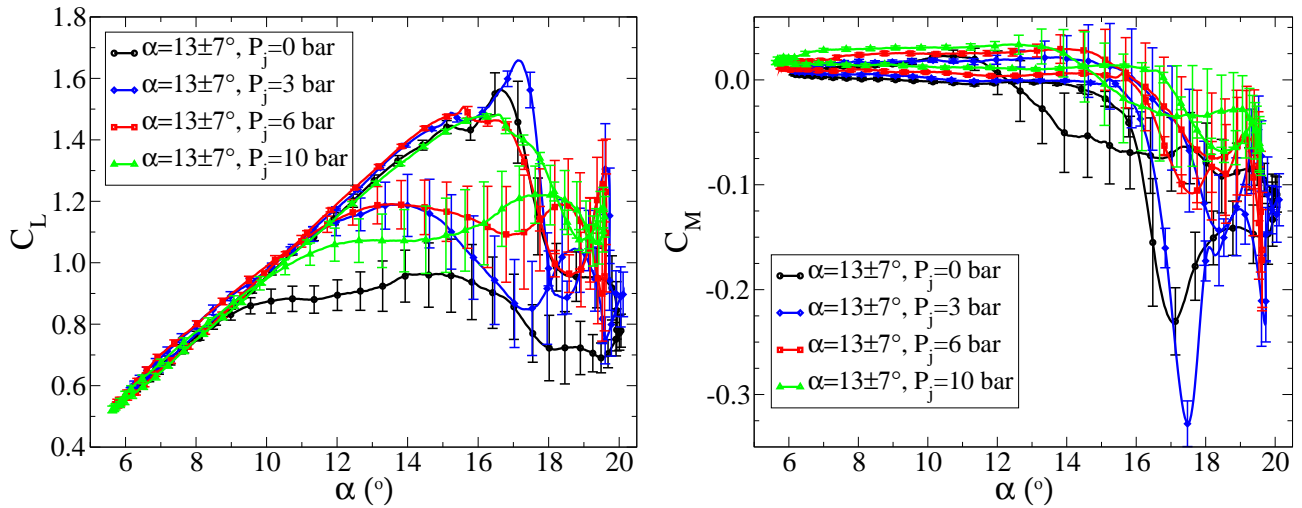


Figure 15: Comparison of lift (Left) and pitching moment coefficient (Right), with and without constant blowing.

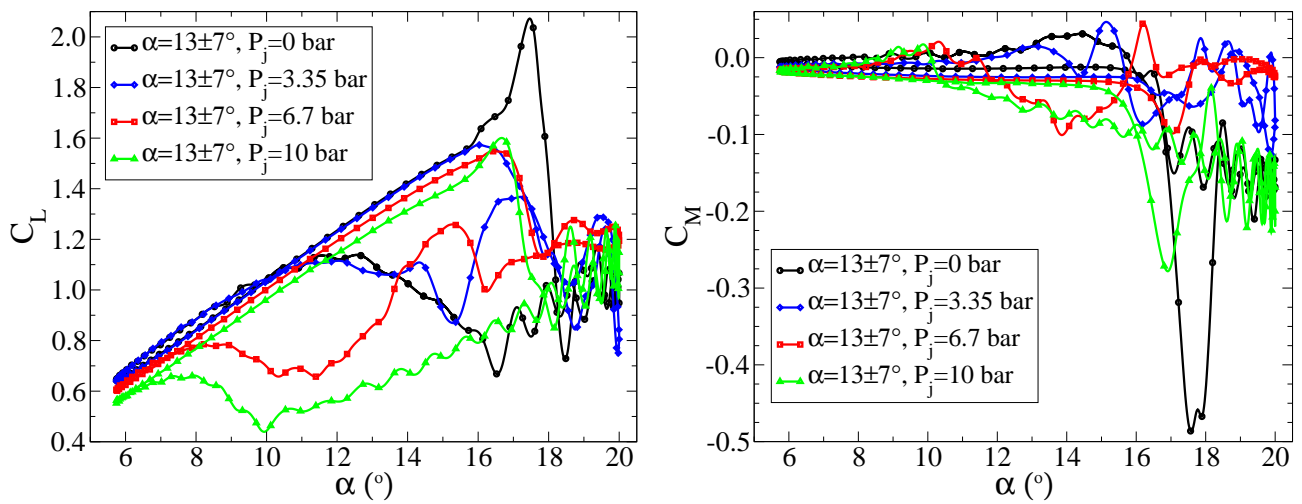


Figure 16: Comparison of URANS computed lift (Left) and pitching moment coefficient (Right) at  $M=0.3$ ,  $Re=1.15e6$ ,  $f=5.7$  Hz ( $\omega^*=0.11$ ),  $\alpha=13\pm 7^\circ$ , with and without constant blowing.

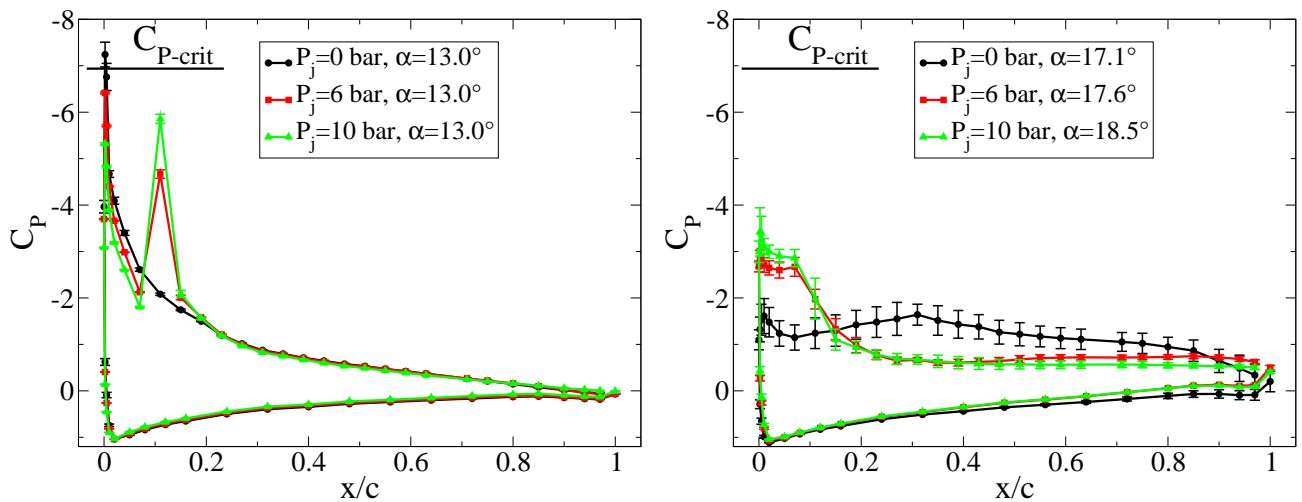


Figure 17: Comparison of pressure coefficient for different blowing pressures at  $M=0.3$ ,  $Re=1.15e6$ ,  $f=5.7$  Hz ( $\omega^*=0.11$ ),  $\alpha=13\pm 7^\circ$  (Left) at constant  $\alpha=13^\circ$  before stall (Right) at minimum pitching moment in the first stall peak.

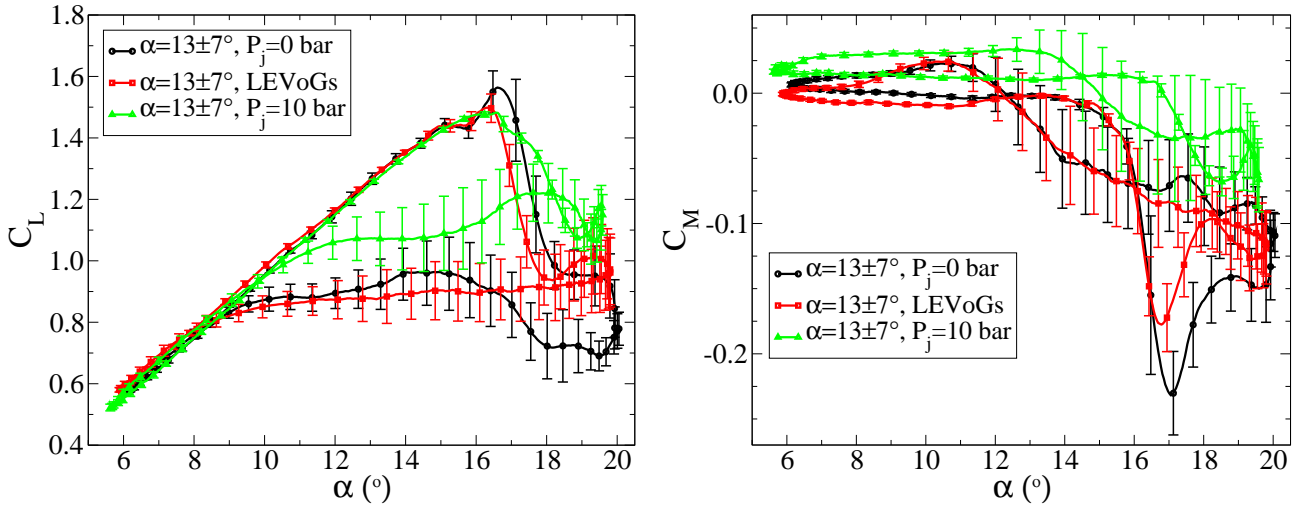


Figure 18: Comparison of lift (Left) and pitching moment coefficient (Right) at  $M=0.3$ ,  $Re=1.15e6$ ,  $f=5.7$  Hz ( $\omega^*=0.11$ ),  $\alpha=13\pm 7^\circ$ , with and without constant blowing compared with flow control by LEVOGs.

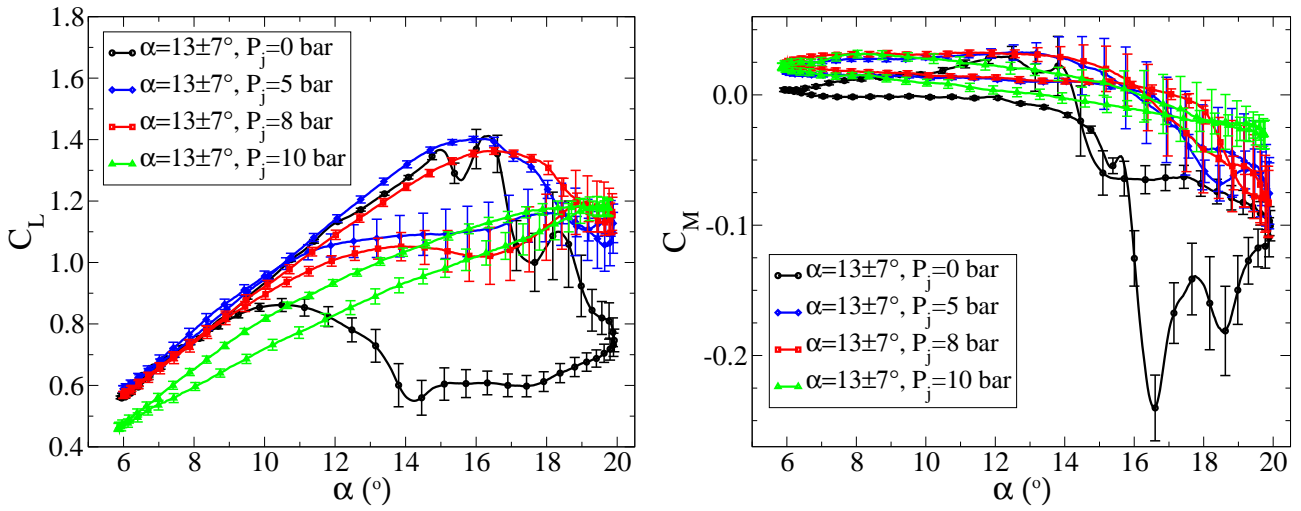


Figure 19: Comparison of lift (Left) and pitching moment coefficient (Right) at  $M=0.3$ ,  $Re=575000$ ,  $f=5.7$  Hz ( $\omega^*=0.11$ ),  $\alpha=13\pm 7^\circ$ , with and without constant blowing.

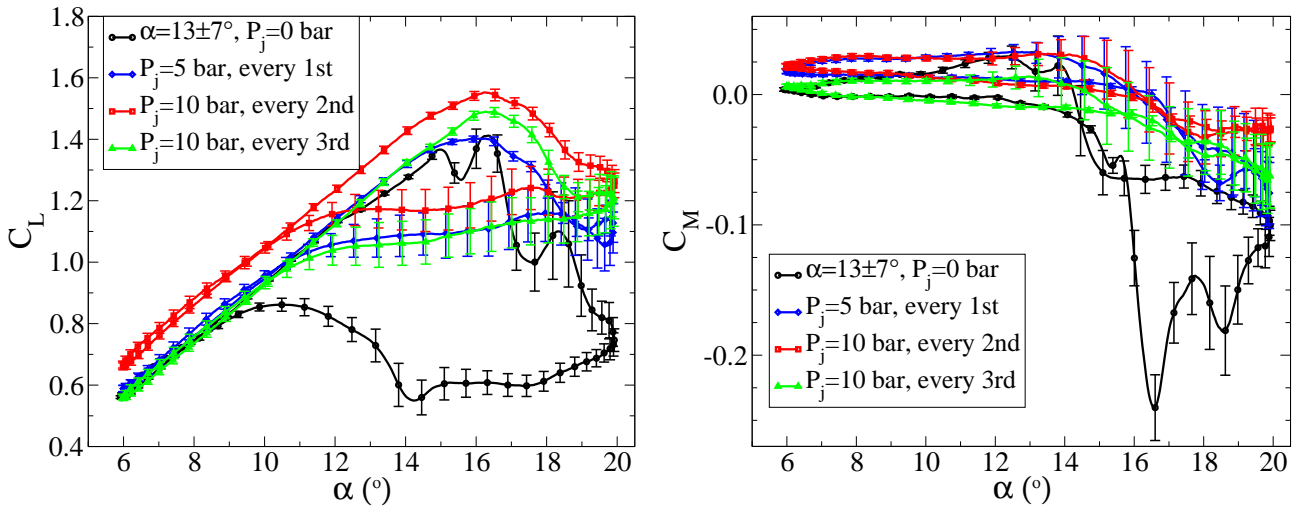


Figure 20: Comparison of the effect of the jet spacing with constant blowing on lift (Left) and pitching moment coefficient (Right) at  $M=0.3$ ,  $Re=575000$ ,  $f=5.7$  Hz ( $\omega^*=0.11$ ),  $\alpha=13\pm 7^\circ$ .

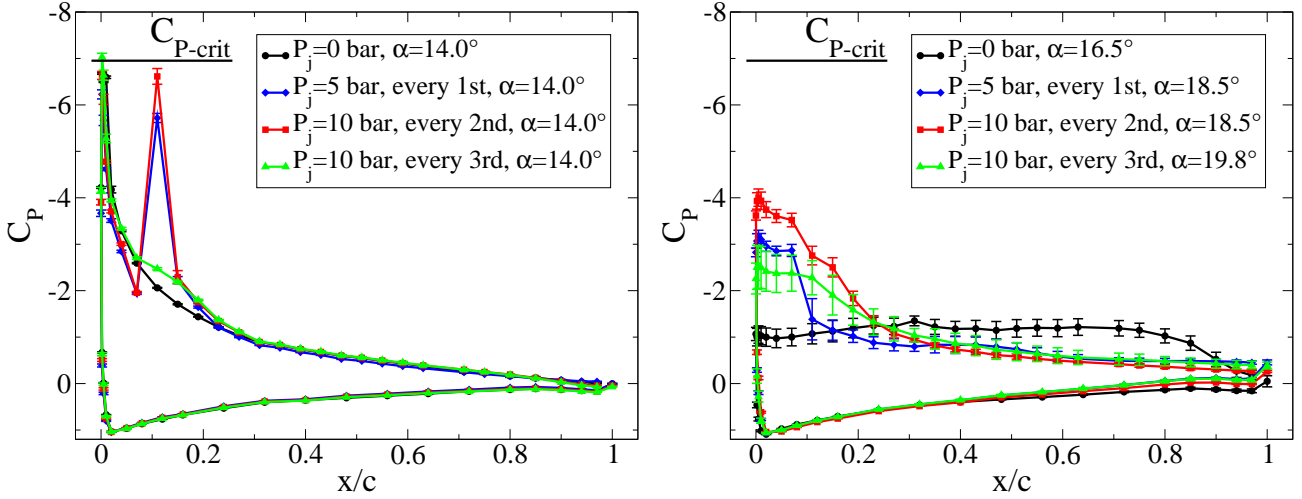


Figure 21: Comparison of pressure coefficient for different jet spacings at  $M=0.3$ ,  $Re=575000$ ,  $f=5.7$  Hz ( $\omega^*=0.11$ ),  $\alpha=13\pm 7^\circ$  (Left) a constant  $\alpha=13^\circ$  before stall (Right) at minimum pitching moment in the first stall peak.

Reynolds number, due mainly to the pronounced kink in the lift curve at  $\alpha=12^\circ$ , which has been shown in other experiments [7] to be the point at which the boundary layer transition on the top of the airfoil reaches the leading edge and stops moving with angle of attack. In addition, the stall occurs  $\Delta\alpha=-1^\circ$  lower in angle of attack than at the higher Reynolds number, and the maximum lift is reduced by 27%. Despite these differences, the pitching moment peak is of comparable size.

At  $P_j=5$  bar ( $C_\mu=0.12$ ,  $C_q=0.019$ ), the pitching moment peak is 65% reduced from the reference case while the peak lift remains similar to the reference case and the mean lift increased by 7%. Both the mean lift and pitching motion peak are worse for both  $P_j=4$  bar and  $P_j=6$  bar (not shown), indicating saturation of the dynamic stall control effect at  $P_j=5$  bar. The dynamic stall control reduces slowly in effectiveness until  $P_j=8$  bar ( $C_\mu=0.20$ ,  $C_q=0.030$ ), which still has a reduction in the pitching moment peak of 61% and an increase in the mean lift of 21%. Starting at  $P_j=5$  bar, the peak lift starts to reduce, until it is 3.5% reduced for  $P_j=8$  bar. At higher pressures, the maximum lift diminishes rapidly, until at  $P_j=10$  bar ( $C_\mu=0.25$ ,  $C_q=0.038$ ), (Figure 19) the maximum lift is reduced by 16% and there is no dynamic stall. For this case, the peak in the pitching moment is effectively completely removed. Interestingly, even in the case where the peak lift is reduced, the lack of stall means that the mean lift over a cycle is still 9% higher than in the case with no blowing. As such, there are two “optimum” amounts of blowing for this Mach number and arrangement of jets: for low dynamic loading  $C_\mu=0.25$  ( $C_q=0.038$ ) and for high performance  $C_\mu=0.12$  ( $C_q=0.019$ ).

Finding the optimal spacing of the jets is more difficult since the maximum mass flux is more strongly limited by the maximum 10 bar total pressure of the jet system. The jet spacing was increased from using every jet ( $s=6.7\%$ ,  $c=20$  mm) to using every second jet ( $s=13.4\%$ ,  $c=40$  mm) or using every third jet ( $s=20.1\%$ ,  $c=60$  mm), as shown in Figure 20. No saturation of the flow control effect was

found with the wider spacings, so the results at the maximum pressure of  $P_j=10$  bar are shown. For the case using every jet, the pressure for which saturation was achieved,  $P_j=5$  bar is shown. The data with every jet at  $P_j=5$  bar ( $C_\mu=0.12$ ,  $C_q=0.019$ ) has approximately the same mass flux as that with every second jet at  $P_j=10$  bar ( $C_\mu=0.12$ ,  $C_q=0.019$ ), but with every second jet the pitching moment peak reduction is 84% as opposed to the 64% peak reduction seen for blowing with every valve. In Figure 20 (Right) for the case using every third jet at  $P_j=10$  bar ( $C_\mu=0.08$ ,  $C_q=0.013$ ), the reduction in the pitching moment peak is 76%, although now the first and second pitching moment peaks are joined. The increase in the lift peak for the case with every third jet is particularly clear in Figure 20 (Left), although an increase is present for all three spacings, and the post-stall lift is improved by a similar amount for all three cases. All three blowing cases have trailing edge stall, with good preservation of the suction peak in front of the jets during and after stall.

The offset in the lift for the case using every second jet is significantly higher than all other cases. In Figure 21 (Left) for attached flow at  $\alpha=14^\circ$  the additional lift for the case with every second jet is due to the additional height of the peak around the jet. When every third jet is used, the pressure peak near the jets disappears entirely in Figure 20 (Left), which is the reason for the lower lift in the attached flow region (Figure 21, Left). The reason for this is that the pressure distribution passes close to jet number 22 (as shown in Figure 5), which is on when every jet is used, or every second jet, but which is turned off when every third jet is used. If the pressure peak due to the jets were present in the data, it would further reduce the height of the pitching moment peak, and as such the pitching moment peak reduction of 76% is probably conservative for the case using every third jet. Thus, although the mean lift is increased by 37% for the case with every second jet and by 25% for the case with every second jet, these values must be treated with some caution. For the pressures available in this ex-

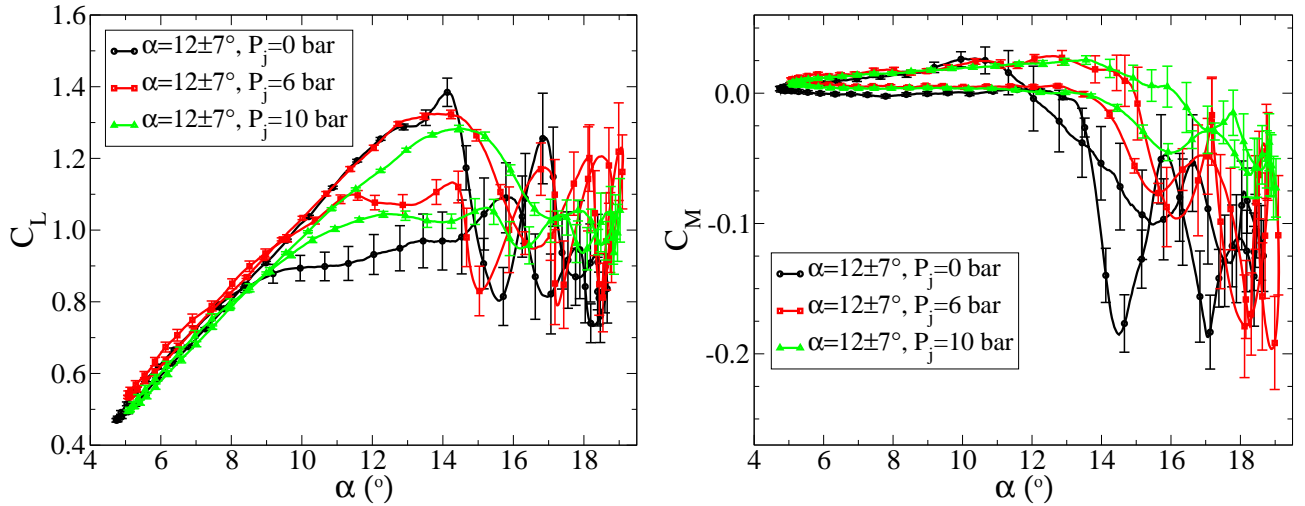


Figure 22: Comparison of lift (Left) and pitching moment coefficient (Right) at  $M=0.4$ ,  $Re=1.5e6$ ,  $f=5.7$  Hz ( $\omega^*=0.08$ ),  $\alpha=12\pm 7^\circ$ , with and without constant blowing.

periment, the optimal jet spacing was  $s=13.4\%$  ( $c=40$  mm) for the maximum effect. Although  $s=20.1\%$  ( $c=60$  mm) has the most efficient use of air pressure it is assumed that this form of flow control would only be used for short periods, and thus efficiency is a secondary consideration.

## STALL AT MACH 0.4 AND 0.5

At higher Mach numbers, the effect of other flow control methods has been variable. The LEVoGs of Mai et al. [13] noted a control effect with slightly reduced effectiveness at Mach 0.4, and the vortex generator and glove approach of Martin et al [14] showed good control at Mach 0.3, but was counterproductive when shocks appeared in the flow for Mach numbers between 0.4 and 0.5, depending on the pitching motion used.

For the constant blowing at Mach 0.4 (Figure 22) the dynamic stall control effect is similar to that at Mach 0.3. At  $M=0.4$ , the mean angle of attack was reduced to 12 degrees so that the flow at mean angle of attack was attached, aiding the adaption of the test section walls. Strong shocks appear in the flow, but the initial stall behaviour remains a typical leading edge stall, similar to that seen at Mach 0.3. For the clean case, a second stall peak, similar in size to the first stall peak appears, also with typical leading edge stall. At  $P_j=6$  bar ( $C_\mu=0.030$ ,  $C_q=0.0060$ ), a double stall is seen, but the initial stall is trailing edge stall, followed by a stronger leading edge stall, much as at  $M=0.3$ . At  $P_j=10$  bar ( $C_\mu=0.050$ ,  $C_q=0.010$ ), the airfoil has only trailing edge stall, and a strong dynamic stall control effect is seen.

In Figure 22 (Right) for  $M=0.4$ , the pitching moment peak is reduced by 59% for  $P_j=10$  bar, while the mean lift over a cycle is increased by 4%. Unfortunately the peak lift is reduced by 7% at this test condition. In Figure 23 (Left), for the attached flow the jets cause a reduction in lift, and the change in effective angle of attack can be seen

on the lower side of the airfoil. In addition, the flow over the pressure sensor near the jets is now supersonic, indicating an expansion of the supersonic part of the flow near jet number 22. At higher angle of attack Figure 23 (Right), a suction plateau at subsonic Mach number is maintained in front of the jets at  $P_j=10$  bar, leading to a significantly higher lift in the separated flow and reducing the negative pitching moment of the airfoil.

At Mach 0.5, the mean angle of attack was reduced to 11 degrees so that the flow at mean angle of attack was attached. For the flow at Mach 0.5 (Figure 24), the flow in the clean case is distinguished by a strong shock (Figure 25, Left), first appearing on the upstroke at  $\alpha=7.5^\circ$ . Shock-induced separation starts at around  $\alpha=11^\circ$ , and the presence of the shocks means that the suction peak is partially preserved and the lift remains high on the airfoil (Figure 25, Right). The pitching moment does not have the sudden peak seen in the flow at lower Mach numbers, and although the pitching moment coefficient is lower than at  $M=0.3$ , the absolute value of the pitching moment peak is 64% higher than for  $M=0.3$ . With blowing, the lift in the attached flow decreases, and a kink in the lift polar appears (For  $P_j=6$  bar at  $\alpha=8.8^\circ$ ) as the first supersonic region appears. There are two supersonic regions, one in the suction peak, then a shock and a second supersonic region around the jet (Figure 25, Left).

After separation, the flow for  $P_j=6$  bar ( $C_\mu=0.015$ ,  $C_q=0.0038$ ) becomes more unsteady and a reduction in the pitching moment peak of 14% is achieved, but the mean lift is reduced by 5% and the peak lift by 4% (Figure 24). At  $P_j=10$  bar ( $C_\mu=0.025$ ,  $C_q=0.0063$ ), the supersonic region behind the jets is stronger than in the suction peak (Figure 25, Left), and after stall, a strongly supersonic region is maintained in front of the jets, which preserves the lift and reduces the negative pitching moment (Figure 25, Right). This results in a reduction of the minimum pitching moment by 61%, although the mean lift is reduced by 4% and the peak lift by 9%. For  $P_j=10$  bar the flow near

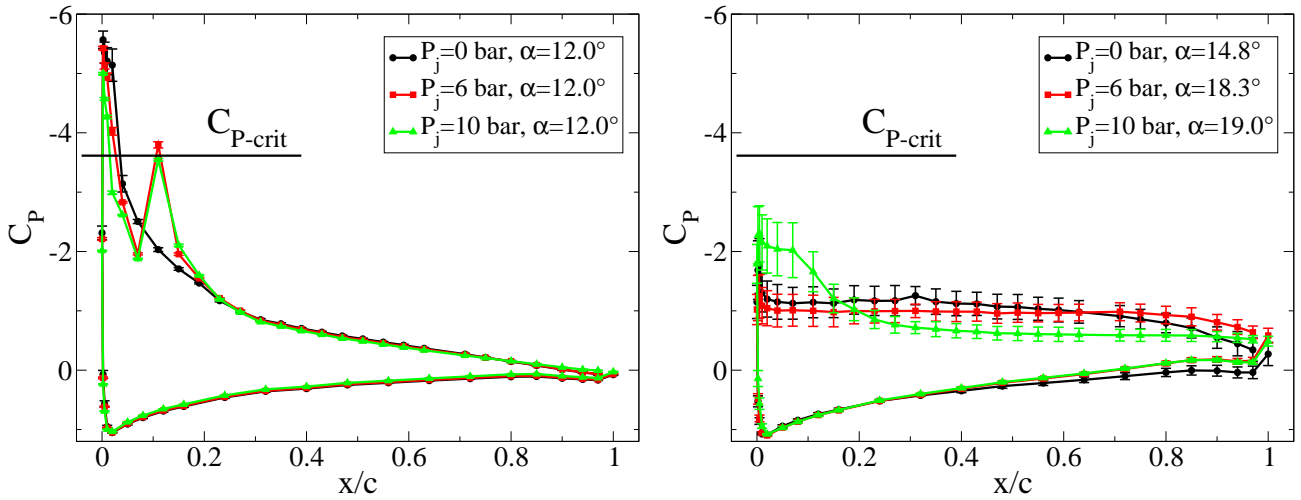


Figure 23: Comparison of pressure coefficient for different blowing pressures at  $M=0.4$ ,  $Re=1.5e6$ ,  $f=5.7$  Hz ( $\omega^*=0.08$ ),  $\alpha=12\pm 7^\circ$  (Left) At constant angle of attack  $\alpha=12^\circ$  before stall (Right) at the point of minimum pitching moment.

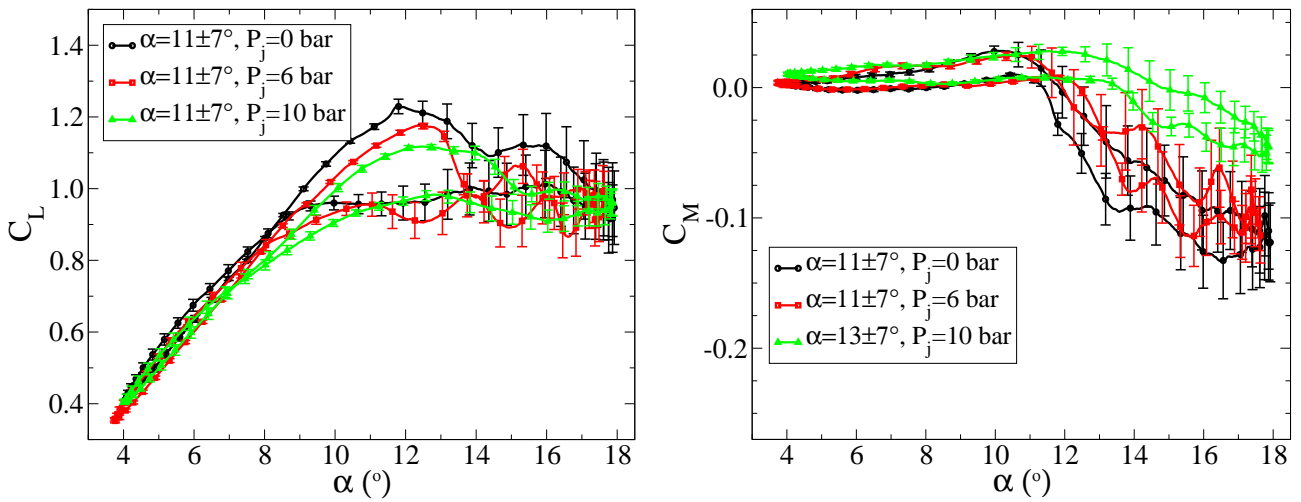


Figure 24: Comparison of lift (Left) and pitching moment coefficient (Right) at  $M=0.5$ ,  $Re=1.9e6$ ,  $f=5.7$  Hz ( $\omega^*=0.06$ ),  $\alpha=11\pm 7^\circ$ , with and without constant blowing.

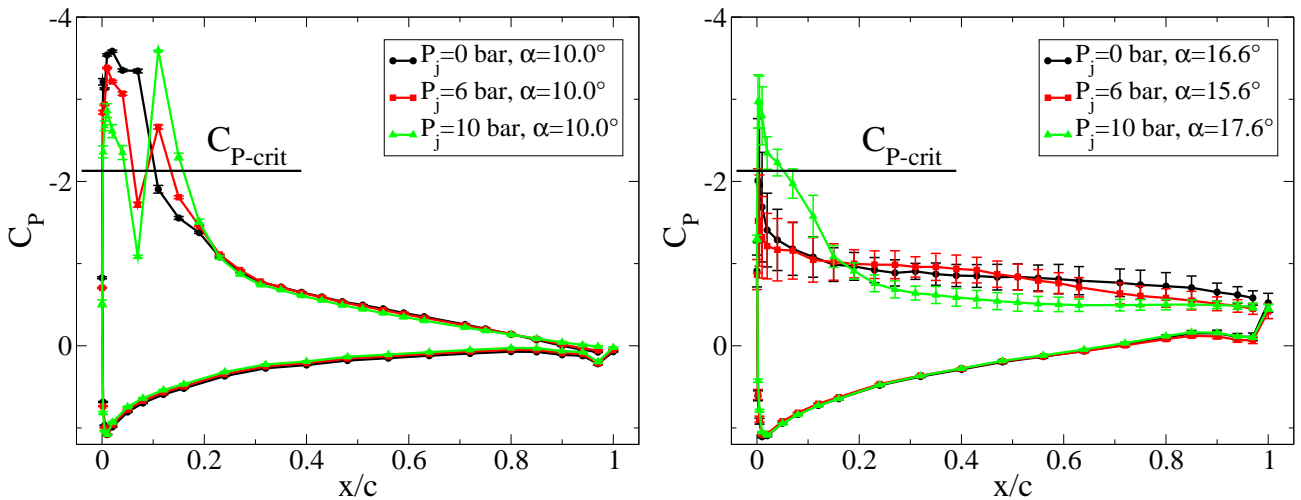


Figure 25: Comparison of pressure coefficient for different blowing pressures at  $M=0.5$ ,  $Re=1.9e6$ ,  $f=5.7$  Hz ( $\omega^*=0.06$ ),  $\alpha=11\pm 7^\circ$  (Left) at constant  $\alpha=10^\circ$  before stall (Right) at minimum pitching moment in the first stall peak.

the jets is always supersonic, and the kink in the lift polar in Figure 25 (Left) is associated with the formation of the supersonic region with a shock in the suction peak.

The dynamic stall control effect at  $M=0.4$  and  $M=0.5$  is less than at  $M=0.3$ , and due to the limitation of the pressure system, no saturation of the dynamic stall control effect was found. Despite these shortcomings, the stall control is good, and no critical Mach number dependence was found. Thus no sudden change in the flow control effectiveness is to be expected if the jets were to be positioned sub-optimally along the radius of a rotor blade.

## AMPLITUDE AND FREQUENCY EFFECT

The conditions tested up to this point in the paper have been for deep dynamic stall. A set of points was also measured to determine the effect of pitching amplitude and pitching frequency on the stall. With this aim, the pitching frequency was reduced at  $M=0.3$ ,  $Re=1.15e6$ ,  $\alpha=13\pm7^\circ$ , measuring  $f=5.75, 5, 4, 3$  Hz, with the effect that for cases without blowing the pitching moment peak was reduced as frequency was reduced, similarly to other experiments [7]. The maximum reduction of 37% was found for  $f=3$  Hz. The pitching moment peaks with blowing at  $P_j=10$  bar remained approximately the same, regardless of frequency, meaning that the relative pitching moment peak reduction was highest for the highest frequency tested.

Amplitude was varied at constant mean angle of attack measuring  $\alpha=13\pm7^\circ, \pm6^\circ, \pm5^\circ, \pm4^\circ$ , with the effect that for deep stall cases the control effect was similar to that shown for  $\alpha=13\pm7^\circ$  and for clean cases a similar reduction in pitching moment peak was seen as for the frequency variation due to the reduction in angular velocity. For  $\alpha=13\pm4^\circ$ , the stall is no longer so deep, and the pitching motion reaches the maximum angle of attack shortly after stall. In this case, the effect of the jets with blowing at  $P_j=10$  bar to delay and slow stall means that the airfoil never fully goes into deep stall. In Figure 26 the pitching moment peak is reduced for this case by 80%, with an increase of the mean lift by 15% and a decrease in the peak lift by 2%.

It is probable that the dynamic stall control efficiencies found for deep dynamic stall represent a lower boundary of efficiency, and that these will be considerably improved for light stall. The stall control is good for a range of amplitudes and frequencies, indicating no critical dependence on the local blade motion.

## 3D DYNAMIC STALL

Previous numerical investigations [6] have indicated that for a 3D airfoil undergoing dynamic stall, that even a relatively small pressure gradient across the breadth of the airfoil causes the stall vortex to be curved, rather than normal to the flow. As seen in that investigation, curvature of the vortex causes a reduction in the height of the lift and

pitching moment peaks, by reducing the strength of the dynamic stall vortex on the centerline of the model. To investigate this effect, the wind tunnel model was equipped with a line of sensors at constant  $x/c=0.51$  and  $x/c=0.80$ , starting at the centerline ( $y/c=0$ ) and extending towards the wind tunnel side-wall ( $y/c=1.67$ ). The measurements are shown in Figure 27 for the test case at  $M=0.3$ ,  $Re=1.15e6$ ,  $f=5.7$  Hz ( $\omega^*=0.11$ ),  $\alpha=13\pm7^\circ$  without blowing, as used in the previous sections of this paper. At  $\alpha=15^\circ$ , the flow has separated at the leading edge, but the flow on the airfoil is still attached and the pressures across the model are quite even. A dynamic stall vortex has formed, and is propagating downstream. At  $\alpha=15.5^\circ$ , the flow at  $x/c=0.51$  at  $y/c=0$  has separated and the pressure has been increased by the downwash-side of the dynamic stall vortex, but the flow at  $x/c=0.51$  further out on the airfoil is still attached, and the pressure is dropping with increasing angle of attack. At  $\alpha=16^\circ$  the pressures in the middle of the airfoil at  $x/c=0.51$  have fallen significantly as the upwash-side of the dynamic stall vortex passes. The pressures at  $x/c=0.80$  have risen as the downwash side of the vortex finally arrives. The flow at this point shows relatively constant flow in the middle of the airfoil out to  $y/c=0.33$ , and the flow near the wind tunnel walls is still attached. This continues as the angle of attack increases to  $\alpha=16.5^\circ$ .

As the angle of attack increases to  $\alpha=17^\circ$ , the pressures at  $x/c=0.80$  begin to fall as they are affected by the upwash side of the dynamic stall vortex. At  $x/c=0.51$ , the pressure at  $y/c=0$  is beginning to rise after the passage of the dynamic stall vortex, while the peak pressure moves toward the wind tunnel wall and the pressure transducers closest to the wall show a pressure drop consistent with flow separation. This continues at  $\alpha=17.5^\circ$ , and it is clear that the dynamic stall vortex has a bowed shape and is furthest downstream in the middle of the airfoil and progressively further upstream at higher  $y/c$ . During the separated flow phase the pressures become much more even than during the separation process, and the reattachment appears to take place evenly over the breadth of the airfoil. The conclusions of the numerical investigations are thus verified.

## CONCLUSIONS

Experiments have been described, showing the dynamic stall control effect of air jets at 10% chord. The effect of blowing at high pressure is to slow the stall and delay the pitching moment peak relative to the initial stall. Additionally, the initial stall is changed from a leading edge to a trailing edge stall, and the suction peak is maintained in front of the jets after stall. This has the effect of reducing the pitching moment peak and increasing the lift after stall. It was found that at Mach 0.3 the optimal blowing mass flux for the jet separation of 6.7% chord was described by  $C_\mu=0.25$  ( $C_q=0.038$ ) for low dynamic loading, with some loss in lift performance, and  $C_\mu=0.12$  ( $C_q=0.019$ ) for maximum reduction in the pitching moment peak without loss

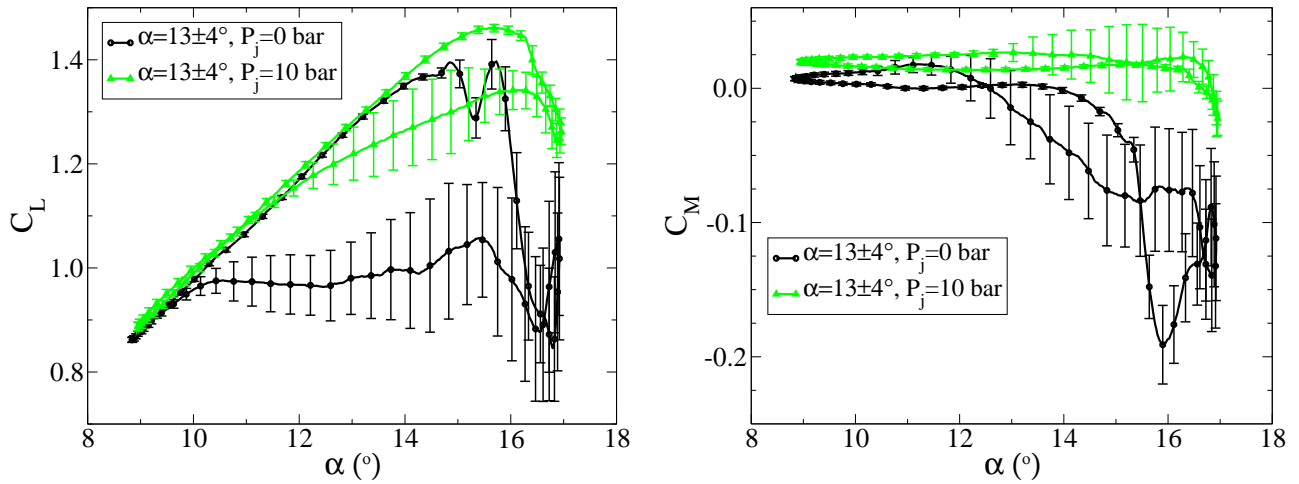


Figure 26: Comparison of lift (Left) and pitching moment coefficient (Right) for light stall at  $M=0.3$ ,  $Re=1.15e6$ ,  $f=5.7$  Hz ( $\omega^*=0.11$ ),  $\alpha=13 \pm 4^\circ$ , with and without constant blowing at  $P_j=10$  bar.

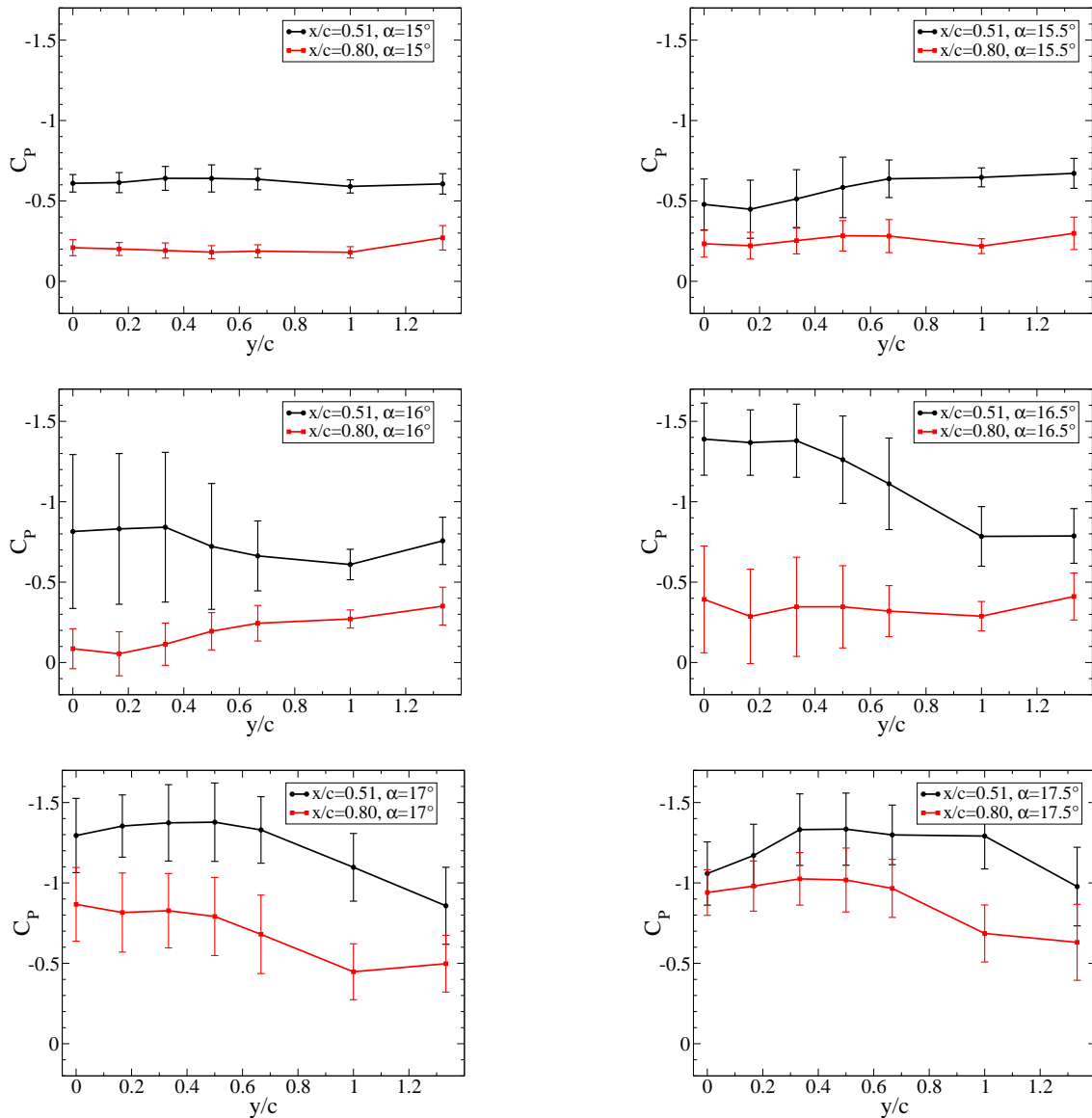


Figure 27: Pressure distributions illustrating the 3D flow during stall at  $M=0.3$ ,  $Re=1.15e6$ ,  $f=5.7$  Hz ( $\omega^*=0.11$ ),  $\alpha=13 \pm 7^\circ$  without blowing.

of lift performance. At these conditions a maximum reduction of the pitching moment peak by 65% was seen, while the peak lift remained similar to the reference case and the mean lift increased by 7%.

Increasing the spacing of the jets resulted in an improvement in the flow control performance, with the best result found with a spacing of 13.3% chord and blowing at  $C_{\mu}=0.12$  ( $C_q=0.019$ ). At this condition a pitching moment peak reduction of 84% was found and the mean lift was increased by 37%. The dynamic stall control effect was found to increase significantly for the few points measured with light stall, due to the stall-delaying effect of the jets.

At Mach 0.4 and 0.5 reductions in the pitching moment peak of 59% and 61% were achieved, respectively. Good dynamic stall control was achieved for cases where high Mach numbers in the suction peak caused shock-induced separation, in contrast to the results found by Martin et al. for blade vortex generators. Unfortunately, the pressure available for the jets was limited, so that no saturation of the control effect was found at these higher Mach numbers.

The three-dimensionality of the dynamic stall without blowing was investigated, showing that the dynamic stall vortex is bowed, curving upstream away from the model centerline. Other investigations using 3D CFD have shown that the dynamic stall measured on this type of model is reduced in strength by 3D effects similar to those measured here. Thus the evidence of the bowed vortex in the experimental results indicates that the dynamic stall strength measured for this experimental arrangement will always be less than for a pure 2D dynamic stall.

## References

- [1] Arnal, D. "Boundary layer transition predictions based on linear theory", Progress in Transition Modelling, AGARD-R-793; 1994.
- [2] www.centaursoft.com
- [3] Costes, M., David, F., Deluc, J.-M., LePape, A., Richez, F., "Experimental Study of Dynamic Stall Control Using Deployable Leading-Edge Vortex Generators", American Helicopter Society 67th Annual Forum, Virginia Beach, VA, May 3-5, 2011.
- [4] Gallot, J., Vingut, G., De Paul, M. V., Thibert, J. "Blade profile for rotary wing of an aircraft", United States Patent 4325675,(20.4.1982).
- [5] Gardner, A.D., Knopp, T., Richter, K., Rosemann, H. "Numerical Investigation of Pulsed Air Jets for Dynamic Stall Control on the OA209 Airfoil", 17th DGLR-Fach Symposium der STAB , 09.-10. Okt. 2010, Berlin, Deutschland.
- [6] Gardner, A.D., Richter K., "Influence of rotation on dynamic stall", American Helicopter Society 68th Annual Forum, Fort Worth, Texas, May 1-3, 2012.
- [7] Gardner, A.D., Richter, K., Mai, H., Altmikus, A.R.M., Klein, A. and Rohardt, C.-H., "Experimental Investigation of Dynamic Stall Performance for the EDI-M109 and EDI-M112 Airfoils", 37th ERF, Gallarate, Varese, 13-15 Sept, 2011.
- [8] Gardner, A.D., Richter, K., Rosemann, H., "Numerical investigation of air jets for dynamic stall control on the OA209 airfoil", CEAS Aeronautical Journal, V. 1, N. 1, 2011. DOI 10.1007/s13272-011-0002-z
- [9] Gerhold, T., Friedrich, O., Evans, J. and Galle, M., "Calculation of Complex Three-Dimensional Configurations Employing the DLR-TAU-Code", AIAA-paper 97-0167, 35th Aerospace Sciences Meeting & Exhibit, Reno, January 6-10, 1997.
- [10] Heine, B., Mulleners, K., Joubert, G., Raffel, M., "Dynamic stall control by passive disturbance generators" 29th AIAA Applied Aerodynamics Conference, 27. - 30. Juni 2011, Honolulu, Hawaii, USA.
- [11] Krumbein, A., Krimmelbein, N., Schrauf, G., "Automatic Transition Prediction in Hybrid Flow Solver, Part 1: Methodology and Sensitivities", Journal of Aircraft, Vol. 46, No. 4, 2009.
- [12] Mack L.M., "Transition prediction and linear stability theory", AGARD Conf. Proc. no 224, Paris, 1977 - Also JPL Publication 77-15, 1977
- [13] Mai, H., Dietz, G., Geissler, W., Richter, K., Bosbach, J., Richard, H., de Groot, K., "Dynamic stall control by leading edge vortex generators", J. Am. Helicopter Soc. 53(1), pp26-36 (2008)
- [14] Martin, P., Wilson, J., Berry, J., Wong, T., Moulton, M., McVeigh, M., "Passive Control of Compressible Dynamic Stall" AIAA Paper 2008-7506, 2008.
- [15] Neuhaus, D., "Ventil", Deutsches Patent DE 199 22 414 (14.5.1999)
- [16] Neuhaus, D., "Magnetisch betätigbares Ventil", Deutsches Patent DE 10 2005 035 878 (31.8.2006).
- [17] Richter, K., Le Pape, A., Knopp, T., Costes, M., Gleize, V., Gardner, A.D., "Improved two-dimensional dynamic stall prediction with structured and hybrid numerical methods," Journal of the American Helicopter Society, Vol. 56, (4), 2011. DOI 10.4050/JAHS.56.042007.
- [18] Traub, L.W., Miller, A., Rediniotis, O., "Effects of Synthetic Jet Actuation Large-amplitude sinusoidal pitching motions" Journal of Aircraft, Vol. 42 No. 1, 2005.
- [19] Weaver, D., McAlister, K.W., Tso, J., "Control of VR7 Dynamic stall by strong steady blowing", Journal of Aircraft, Vol. 41, No. 6, 2004.